Nanomedicine: Nanotechnology, Biology, and Medicine
14 (2018) 483–491

nanomedjournal.com

Multimodal imaging for a theranostic approach in a murine model of B-cell lymphoma with engineered nanoparticles

Enza Torino, PhD[a,b,c,1], Luigi Auletta, PhD, DVM[d,1], Donatella Vecchione, PhD[a,c], Francesca Maria Orlandella, PhD[d], Giuliana Salvatore, PhD, MD[d,e], Enrico Iaccino, PhD[f], Dario Fiorenza, DVM, PharmD[d], Anna Maria Grimaldi, PhD[d], Annamaria Sandomenico, PhD[g], Sandra Albanese, PhD[g], Daniela Sarnataro, PhD[h,i], Matteo Gramanzini, DVM[g], Camillo Palmieri, PhD[f], Giuseppe Scala, PhD, MD[f], Ileana Quinto, PhD, MD[f], Paolo Antonio Netti, PhD[a,b,c], Marco Salvatore, MD[d], Adelaide Greco, PhD, DVM[j,g,h,*]

[a]*Istituto Italiano di Tecnologia, IIT - Center for Advanced Biomaterials for Health Care, CABHC@CRIB, Napoli, Italia*
[b]*Centro Interdipartimentale di Ricerca sui Biomateriali, Università degli Studi di Napoli Federico II, Napoli, Italia*
[c]*Dipartimento di Ingegneria Chimica, dei Materiali e della Produzione Industriale, Università degli Studi di Napoli Federico II, Napoli, Italia*
[d]*IRCCS SDN S.p.A., Napoli, Italia*
[e]*Dipartimento di Scienze Motorie e del Benessere, Università "Parthenope", Napoli, Italia*
[f]*Dipartimento di Medicina Sperimentale e Clinica, Università degli Studi "Magna Graecia" di Catanzaro, Catanzaro, Italia*
[g]*IBB, CNR, Napoli, Italia*
[h]*CEINGE Biotecnologie Avanzate, s.c.ar.l., Napoli, Italia*
[i]*Dipartimento di Medicina Molecolare e Biotecnologie Mediche, Università degli Studi di Napoli Federico II, Napoli, Italia*
[j]*Dipartimento di Scienze Biomediche Avanzate, Università degli Studi di Napoli Federico II, Napoli, Italia*

Received 26 July 2017; accepted 13 November 2017

Abstract

Nanoparticles (NPs) are a promising tool for *in vivo* multimodality imaging and theranostic applications. Hyaluronic acid (HA)-based NPs have numerous active groups that make them ideal as tumor-targeted carriers. The B-lymphoma neoplastic cells express on their surfaces a clone-specific immunoglobulin receptor (Ig-BCR). The peptide A20-36 (pA20-36) selectively binds to the Ig-BCR of A20 lymphoma cells. In this work, we demonstrated the ability of core-shell chitosan-HA-NPs decorated with pA20-36 to specifically target A20 cells and reduce the tumor burden in a murine xenograft model. We monitored tumor growth using high-frequency ultrasonography and demonstrated targeting specificity and kinetics of the NPs *via in vivo* fluorescent reflectance imaging. This result was also

Abbreviations: HA, Hyaluronic acid; NPs, nanoparticles; Ig-BCR, immunoglobulin B-cell receptor; pA20-36, peptide A20-36; pCNT, scrambled or control peptide; MRI, magnetic resonance imaging; FRI, fluorescent reflectance imaging; Ch, chitosan; Mw, molecular weight; TPP, sodium tripolyphosphate; EtOH, ethanol; Gd-DTPA, gadolinium diethylene-triamine-pent-acetate; EDC, 1-ethyl-3-(3-dimethylaminopropyl) carbodiimide hydrochloride; NHS, N-hydroxysuccinimide; pCNT, scrambled control peptide; DVS, divinyl sulfone; PEG, polyethylene glycol; FITC, fluorescein isothiocyanate; Ex/Em, excitation/emission; Cy7, cyanine7; STED, stimulated emission depletion; PBS, phosphate-buffered saline; BCA, Bicinchoninic Acid Protein; OD, optical density; SEM, scanning electron microscope; TEM, transmission electron microscope; DLS, dynamic light scattering; CPC, Carr-Purcell sequence; RPMI, Roswell Park Memorial Institute; HFUS, high frequency ultrasound; SE, standard error of the mean; RM-ANOVA, repeated measures analysis of variance; FlS, fluorescence reflectance signal; DAPI, 4′,6-diamino-2-phenylindole•2HCl.

Competing interest: The authors declare no competing interests.

Funding: This work was supported by Ministero dell'Istruzione, dell'Università e della Ricerca to A. Greco (PRIN project 2012CK5RPF_006), I. Quinto and G. Scala (PRIN project 2012CK5RPF; PRIN project 2012CK5RPF_002).

*Corresponding author at: Dipartimento di Scienze Biomediche Avanzate, Università degli Studi di Napoli Federico II, Napoli, Italia.
E-mail address: adegreco@unina.it (A. Greco).

[1] These authors contributed equally to this work.

https://doi.org/10.1016/j.nano.2017.11.016

confirmed by *ex vivo* magnetic resonance imaging and confocal microscopy. In conclusion, we demonstrated the ability of NPs loaded with fluorescent and paramagnetic tracers to act as multimodal imaging contrast agents and hence as a non-toxic, highly specific theranostic system.

Key words: Mouse model; Preclinical imaging; Theranostic; Fluorescence imaging; Magnetic resonance; Engineered nanoparticles

Lymphoproliferative diseases such as lymphoma and multiple myeloma are characterized by clonal expansion of neoplastic B-cells, which produce immunoglobulins that can be detected in serum and/or in urine.[1–3] On its surface, each neoplastic clone expresses the immunoglobulin B-cell receptor (Ig-BCR). The Ig-BCR hypervariable regions are derived from immunoglobulin gene rearrangement and are unique for each tumor B-cell clone.[4] Hence, Ig-BCR can be considered a highly specific tumor marker and an ideal target for tumor-specific therapeutic approaches with the objective of reducing the harmful effects associated with conventional anticancer therapies.[4]

To selectively target tumor-specific markers, several approaches have been used, and among these, mimotopes are particularly interesting. Mimotopes are amino-acidic sequences, *i.e.*, peptides, that are able to mimic the three-dimensional structure of the original antigenic epitope.[5] Their use represents an attractive alternative for immunotherapy of lymphoproliferative disorders triggered by cross-linking with the cancer-associated surface receptors.[4,6,7] Hence, mimotopes can be conjugated to a variety of molecules and act as vehicles for therapeutic agents as well as vehicles for molecular imaging agents with extreme specificity towards tumor cells.[4,8,9] Previously, a specific mimotope, namely, peptide A20-36 (pA20-36), was selected from other available peptides for its selective binding to the Ig-BCR of B-cell lymphoma (A20) cells. Furthermore, the pA20-36 ability to induce apoptosis in a caspase-dependent manner was demonstrated.[4]

Preclinical molecular imaging is a fundamental tool for *in vivo* testing of the efficacy of selected targets for both diagnosis and therapy in mouse models of human disease. Multimodal preclinical imaging is considered an advancement of each single imaging modality because it allows the integration of morphological and functional information.[10–12] For example, the combination of high-field magnetic resonance (MRI) and fluorescence reflectance imaging (FRI) leverages the high speed and sensitivity of the latter technique with the high anatomic resolution and soft tissue contrast of MRI.[13] The translation of such a multimodal system into the human clinical routine represents a newly desirable and current challenge, primarily because of the non-invasiveness of the techniques.

Nanotechnologies such as nanoparticles (NPs) represent a promising tool for *in vivo* multimodality imaging and might also allow for theranostic application, *i.e.*, fusion of targeted imaging and therapy in a single molecule.[13–18]

The current work developed a new personalized B-cell lymphoma therapy based on a site-specific receptor-mediated drug delivery system. Specifically, core-shell chitosan-hyaluronic acid NPs with improved relaxometric properties were decorated with pA20-36 to actively target the specific Ig-BCR idiotype on A20 cells.[19] Furthermore, a fluorescent tracer together with a paramagnetic agent were loaded into the NPs to verify the multimodal theranostic potentiality of this molecule *in vivo* in a xenograft mice model of murine B lymphoma.

Methods (refer to the supplementary information for details)

Core-shelled chitosan (Ch) hyaluronic acid (HA) NPs were synthesized using a modified emulsion-coacervation method and characterized. They were than directly conjugated with pA20-36 for *in vitro* and *in vivo* evaluations. *In vivo* experiments were performed in accordance with the European guidelines of the 2010/63/EU Directive on the protection of animals used in scientific studies, after Italian Ministry of Health approval, Protocol no. 49/2015-PR e n° 50/2015-PR.

Results

Preparation and characterization of NPs

The core-shell architecture of NPs obtained by emulsion-coacervation was observed using transmission electron microscopy (TEM). Briefly, a Complex Emulsion-Coacervation is used for the production of Hybrid Core Shell nanostructures. The first step consists in the preparation of a w/o emulsion used as a template. The water phase is made of an aqueous solution of Ch and AcOH 8% v/v obtained by mixing 5 ml of MilliQ water at a Ch concentration ranging from 0.1% wt/v to 1% wt/v. The oil phase is obtained by dissolving the surfactant Span80 (0.5-1% wt/v) in 45 ml of Mineral Oil and homogenizing for 5 min at 7000 rpm (by L5MA purchased by Silverton). The primary emulsion, obtained by mixing both phases, is treated for 20 min at 7000 rpm. Then, the solution containing HA, as a coacervate polymer, is added dropwise and the final volume is homogenized at 7000 rpm for further 30 min, keeping constant the Temperature at 37 °C. In a different preparation, a clinical relevant paramagnetic contrast agent, Gd-DTPA, at a concentration of 18 mM, is added to the aqueous solution containing Ch before mixing to the oil phase. To improve the stability of the coacervate, two crosslinking agents are added to the phases. The effect of the temperature is also tested up to 37 °C. Stable nanoparticles with a narrow particle size distribution are obtained. After bioconjugation with pA20-36, NPs were checked by *in vitro* bench top relaxometer to confirm the MRI capability related to the concentration. Briefly, ICP-MS is used to assess the concentration of Gd-DTPA loaded within the NPs. These data are also used to evaluate the relaxometric properties of the

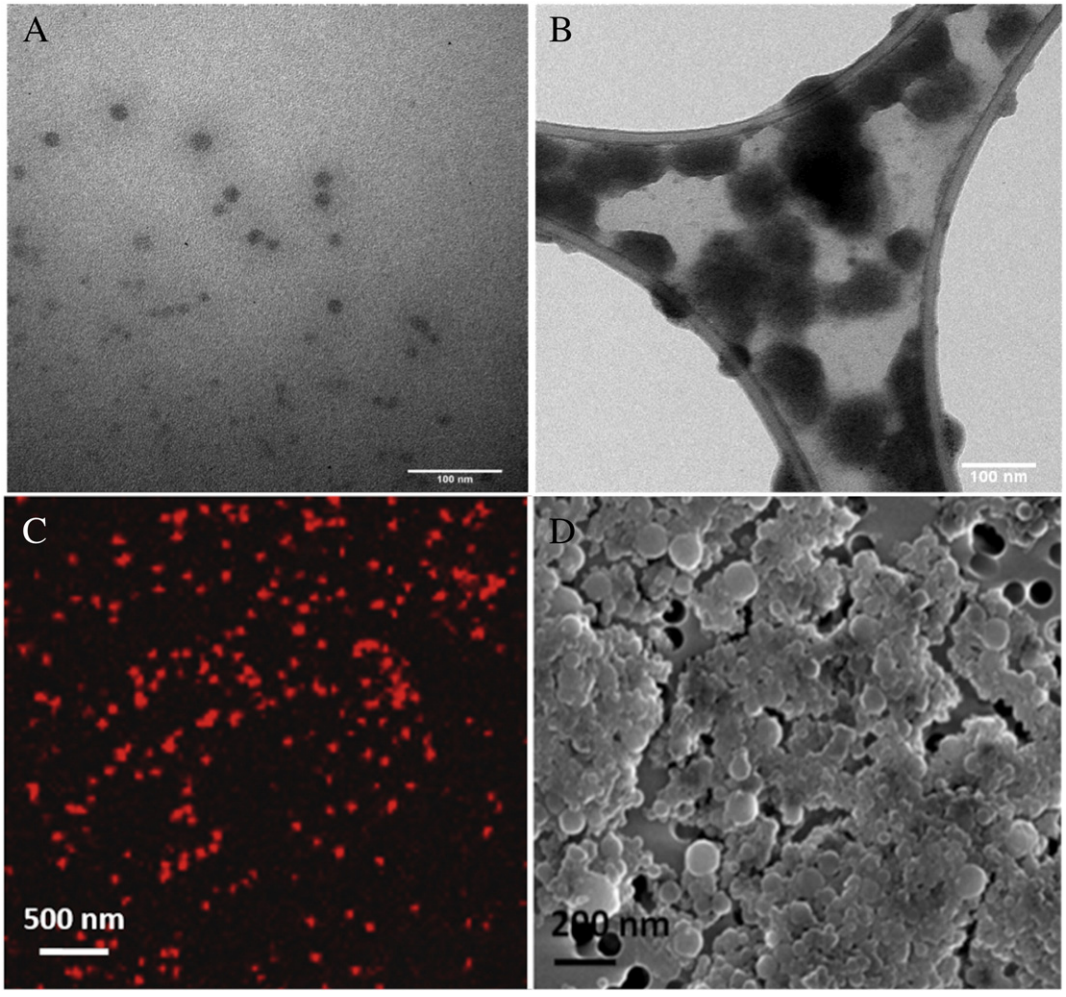

Figure 1. Morphological characterization of nanoparticles (NPs). In (**A**) and (**B**) TEM images in dry-mode of Nanoparticles conjugated with the A20-36 peptide. In (**A**), landscape of naked core-shell nanoparticles. In (**B**), landscape of bioconjugated nanoparticles at low magnification obtained by using a pre-charged grid surface to improve accumulation of the vesicles. In (**C**), super-resolution acquisitions by stimulated emission depletion (STED) of NPs encapsulating ATTO488. In (**D**), SEM observation of core-shell NPs reported in Fig. 1, A.

nanovectors. Results demonstrate that the cargo of the NPs was preserved during the conjugation since the loading was mainly located within the core responsible of the improved relaxometric properties, as previously described.[20] *In vitro* concentration of Gd-DTPA loaded in the NPs with improved relaxometric properties was in the range of 1 mM, even though *ex vivo* homogenization of organs has not been performed to assess the *in vivo* accumulation of the NPs.

A representative TEM image and the corresponding enlargement are presented in Figure 1, *A* and *B*, highlighting the high-density core made of chitosan and the perfect coating of HA that forms the shell. Furthermore, we imaged the core-shell NPs using a specific dye (ATTO488) suitable for stimulated emission depletion (STED) imaging (Figure 1, *C*). Due to the notably reduced size of the nanoparticles, it was impossible to discriminate whether the dye was present within the core or in the shell. The NPs size was measured by DLS at 37 °C performed with a Zeta Nano ZN (Malvern Instruments, UK). Each cuvette was filled with 1 mL of NP suspensions in water (0.1 mg/mL) in a 1:1 (v/v) ratio. Multiple scattering was ruled out by performing analysis in more dilute conditions to avoid the formation of aggregates. The data are the average of three runs of the same sample where the standard deviation was always below 30%. The spherical structure of the NPs was confirmed *via* scanning electron microscope (SEM; Figure 1, *D*), and the NPs size distribution obtained by dynamic light scattering (DLS) analysis reported a zeta average of approximately 70 nm with a polydispersity index of approximately 0.2.

Zeta potential results demonstrated that naked NPs show −45 mV (Standard Deviation ±5 mV) on the slightly positive surface charge of the Chitosan core alone (+15 mV). However, conjugation with A20-36 partially neutralizes the surface charge to −10 mV ± 5 mV.

Bioconjugation of NPs

The NPs were conjugated with polyethylene glycol (PEG), PEG-fluorescein isothiocyanate (FITC) or PEG-cyanine7 (Cy7) according to the analysis to be performed and the instrument

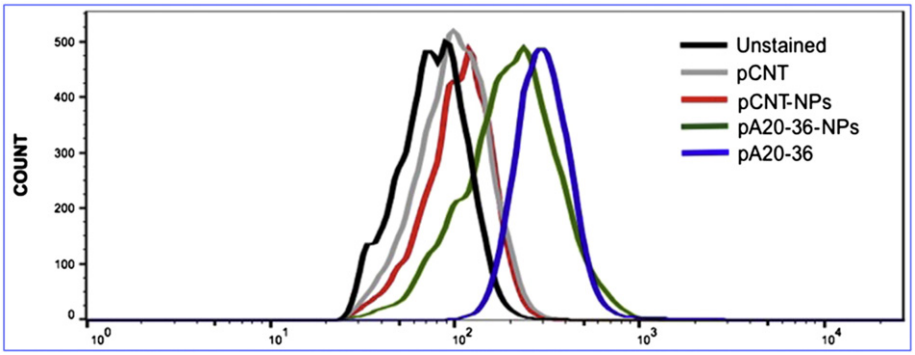

Figure 2. Binding of pA20-36-decorated NPs to A20 cells by flow cytometry. The A20 cells were stained with NPs-FITC decorated with pA20-36 or pCNT. Cells were incubated with pA20-36-FITC or pCNT-FITC as positive and negative controls, respectively. The *y*-axis shows the number of events (counts), *i.e.*, the number of cells with a certain fluorescence intensity, in arbitrary units on the x-axis.

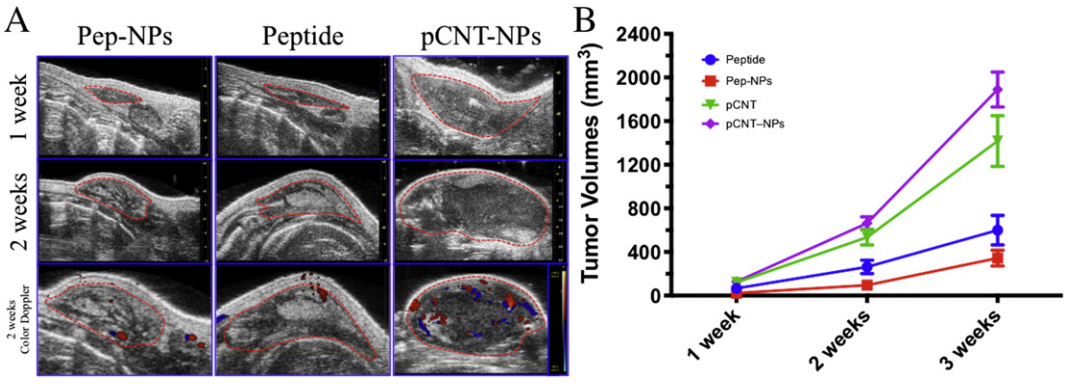

Figure 3. High frequency ultrasonographic (HFUS) evaluation of tumors and their growth curves. (**A**) *In vivo* B- and color-Doppler-mode HFUS of A20-lymphoma cell xenografts. Each column represents a different group, from left to right: pA20-36-NPs, pA20-36 and pCNT-NPs. The first row is the B-mode sagittal acquisition after the first week of treatment, and the second row shows the same after the second week of treatment. The third row shows the color-Doppler acquisition after 2 weeks of treatment at a pulse repetition frequency (PRF) of 4 kHz (flow detection lower limit of up to 48 mm/s). The red dotted line shows the tumor boundaries. (**B**) Graphic representation of the two-way RM-ANOVA showing the tumor volumes in the four treatment groups over time. In red, pA20-36-NPs (pA20-36-decorated NPs) treated group; in blue, pA20-36 alone treated group; in green, pCNT (scrambled peptide) treated group; in purple, pCNT-NPs (scrambled peptide-decorated NPs) treated group.

characteristics. The results of the pH titration for quantitative evaluation of the carboxylic group reported 4 mol/ml of –COOH groups for the NPs. For the NPs (Excitation 650 nm/Emission 680 nm, Ex/Em), the range of concentration detected by spectrofluorimeter was between 1 and 150 μg/ml. In this range, no saturation events of the signal occurred, and the experiments performed at different dilutions confirmed the absence of shielding effects of the NPs. In the purification steps, loss of NPs usually occurs. Indeed, the initial concentration of NPs was 1250 μg/ml, and after purification, the concentration was 1077 μg/ml, confirming the loss of 14% w/v according to the calibration line. The amount of conjugated PEG was measured by comparison of different ratios of the NPs suspension dilutions with a calibration line of PEG-Cy7 (Ex 730 nm/Em 820 nm) in the range of 0-40 nmol/ml. The final concentration was 27.8 nmol/ml with a yield of 68.95% w/v. In the case of NPs, as result of this analysis, a concentration of 26.74 nmol/ml was obtained with a final yield of 66.85% w/v for the NPs.

The NPs were directly conjugated to pA20-36 or a scrambled control peptide (pCNT) through the –COOH groups of the shell after activation with carbodiimide hydrochloride (EDC) and N-hydroxysuccinimide (NHS), as described in supplementary material. The morphology of NPs conjugated with pCNT was similar to that reported for pA20-36. The analysis reported a concentration of 22 nmol/ml after conjugation with pA20-36 peptide with a 73% yield. For the double functionalization of PEG-FITC and peptide, quantification of PEG-Cy7 by spectrofluorimeter and quantification of protein were both performed, and the results were 2 nmol/ml (yield 25%) and 15 nmol/ml (yield 75%), respectively. The particle size distribution was determined by DLS after functionalization to verify that no particle aggregation had occurred.

Specific binding of idiotype pA20-36-decorated NPs to A20 cells

Using flow cytometry, we evaluated the ability of the pA20-36 or control peptide (pCNT)-decorated NPs to bind to A20 cells. The

FITC signals of pCNT-FITC, pCNT-NPs-FITC and unstained A20 cells were quite similar, whereas the pA20-36-FITC and pA20-36-NPs-FITC peaks were higher, confirming that pA20-36 carried the decorated NPs to the target A20 cells (Figure 2).

Effectiveness of therapy with pA20-36-decorated NPs

After the *in vitro* evaluation, the pA20-36-decorated NPs, at a dose of 10 mg/kg of peptide intravenously once per day for two weeks, were used to treat mice bearing subcutaneous xenografts from B-lymphoma A20 cells, and their effect was compared with that of *ad hoc* control molecules. The *in vivo* efficacy experiment was performed in forty Balb/C nude mice, evenly distributed in four treatment groups (see Supplementary Material, *In vivo* studies). The total injected volume was 100 μL per mouse. The amount of fluorophore in 100 μL was about 2.5 nmol as required by the fluorescence equipment. Nanoparticle concentration was 0.1 mg/mL.

The tumor dimensions were obtained on two-dimensional B-mode High frequency ultrasound (HFUS) images (Figure 3, *A*) and tumor volumes were calculated according to (1) (see Supplementary Material, *In vivo* HFUS). The two-way repeated measures analysis of variance (RM-ANOVA) showed a significant difference between treatment groups over time (Figure 3, *B*; $P < 0.0001$). The *post hoc* analysis showed that the pA20-36-NPs ($P < 0.0001$) and pA20-36 ($P = 0.02$) treated mice had smaller tumors compared with the pCNT and pCNT-NPs treated mice after the first week of treatment (23.1 ± 9.2 *vs.* 66.5 ± 15.6 *vs.* 119.9 ± 13.1 *vs.* 127.1 ± 45.7 mm^3, respectively). No difference was detected between the pA20-36-NPs and pA20-36 treated mice ($P = 0.12$) nor between the pCNT and pCNT-NPs treated mice ($P = 0.98$) at one week. Similar results were obtained after the second week (Figure 3, *B*). Indeed, at the end of the second week of treatment, a significant difference was detected between the pA20-36-NPs ($P < 0.0001$) and pA20-36 ($P = 0.001$) treated mice compared with pCNT and pCNT-NPs treated mice (95.7 ± 46.6 *vs.* 262.6 ± 62.1 *vs.* 535.0 ± 70.7 *vs.* 663.9 ± 57.6 mm^3, respectively), but no difference was noted between the pA20-36-NPs and pA20-36 treated mice ($P = 0.22$) or between the pCNT and pCNT-NPs treated mice ($P = 0.44$). The effect of the therapy on the tumor volumes was still evident after one week of interruption, with pA20-36-NPs ($P < 0.0001$) and pA20-36 ($P = 0.005$) treated mice bearing smaller tumors compared with both pCNT and pCNT-NPs treated mice (343.6 ± 72.7 *vs.* 600.0 ± 135.8 *vs.* 1416.9 ± 232.8 *vs.* 1889.8 ± 159.9 mm^3, respectively). However, no significant difference was observed between the pA20-36-NPs and pA20-36 alone treated mice ($P = 0.18$) or between the pCNT and pCNT-NPs treated mice ($P = 0.68$).

Even if not performed quantitatively, the vascularization analysis at a pulse repetition frequency (PRF) of 4 kHz showed a reduced number of blood vessels in the periphery of the tumor and none in the center of the mass in both pA20-36-NPs and pA20-36 treated mice compared with both pCNT and pCNT-NPs treated mice (Figure 3, *A*).

Overall, these results indicate the ability of pA20-36-decorated NPs to slow tumor growth as much as the pA20-36 alone and that this effect persisted after one week of therapy withdrawal.

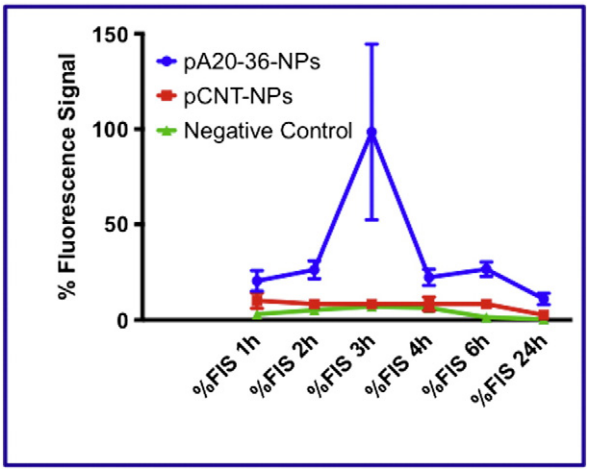

Figure 4. Graphic representation of *in vivo* FRI results. Two-way RM-ANOVA showing the %FIS in the three study groups over time. In blue, pA20-36-NPs; in red, pCNT-NPs; in green, negative control.

Peptide A20-36-decorated NPs as a multimodal imaging agent

We evaluated the capability of pA20-36-decorated NPs for use as a multimodal imaging agent by performing FRI and MRI studies.

The *in vivo* FRI study allowed us to evaluate the pharmacokinetics properties of the NPs loaded with ATTO680. This analysis showed that after 3 h of biodistribution, the FIS% was significantly higher ($P = 0.0001$) with pA20-36-NPs (98.5 ± 46.1) compared with pCNT-NPs (8.4 ± 1.9) and negative control mice (7.1 ± 1.7) (Figure 4, *A*). Although the difference was not significant, the FIS% of pA20-36-NPs was always higher than that of the other two groups at the other time points as well (1-2-4-6-24 h) (Figures 4 and 5; Table 1). Our results demonstrated the ability of FRI to trace fluorescent NPs *in vivo* and to detect the timing of both peak accumulation of NPs and their persistence in the lesion.

Based on the results of the biodistribution studies, *ex vivo* FRI, MRI and confocal microscopy studies were performed on a different subset of four mice after three hours. All techniques confirmed the higher signal with pA20-36-NPs. In particular, *ex vivo* FRI showed a significant difference in signal intensity ($P = 0.03$) between pA20-36-NPs (1150.0 ± 432.9 counts/energy) and both pCNT-NPs (358.3 ± 74.7 counts/energy) and negative control mice (371.5 ± 91.1 counts/energy) (Figure 6, *A*).

For pA20-36-NPs loaded with gadolinium diethylene-triamine-pent-acetate (Gd-DTPA), *ex vivo* MRI showed a signal intensity of 175.1 ± 15.8, which was significantly higher than the signal detected for both pCNT-NPs (85.5 ± 7.9) and negative controls NPs (57.9 ± 10.1) ($P < 0.0001$; Figure 6, *B* and *C*). The latter two groups were not significantly different. *Ex vivo* confocal microscopy confirmed these data (Figure 7).

Discussion

Nanoparticles (NPs) have been used in a wide number of *in vivo* preclinical studies, and their ability to function as both multimodal imaging agents and as theranostic agents has been demonstrated in several types of murine models of human

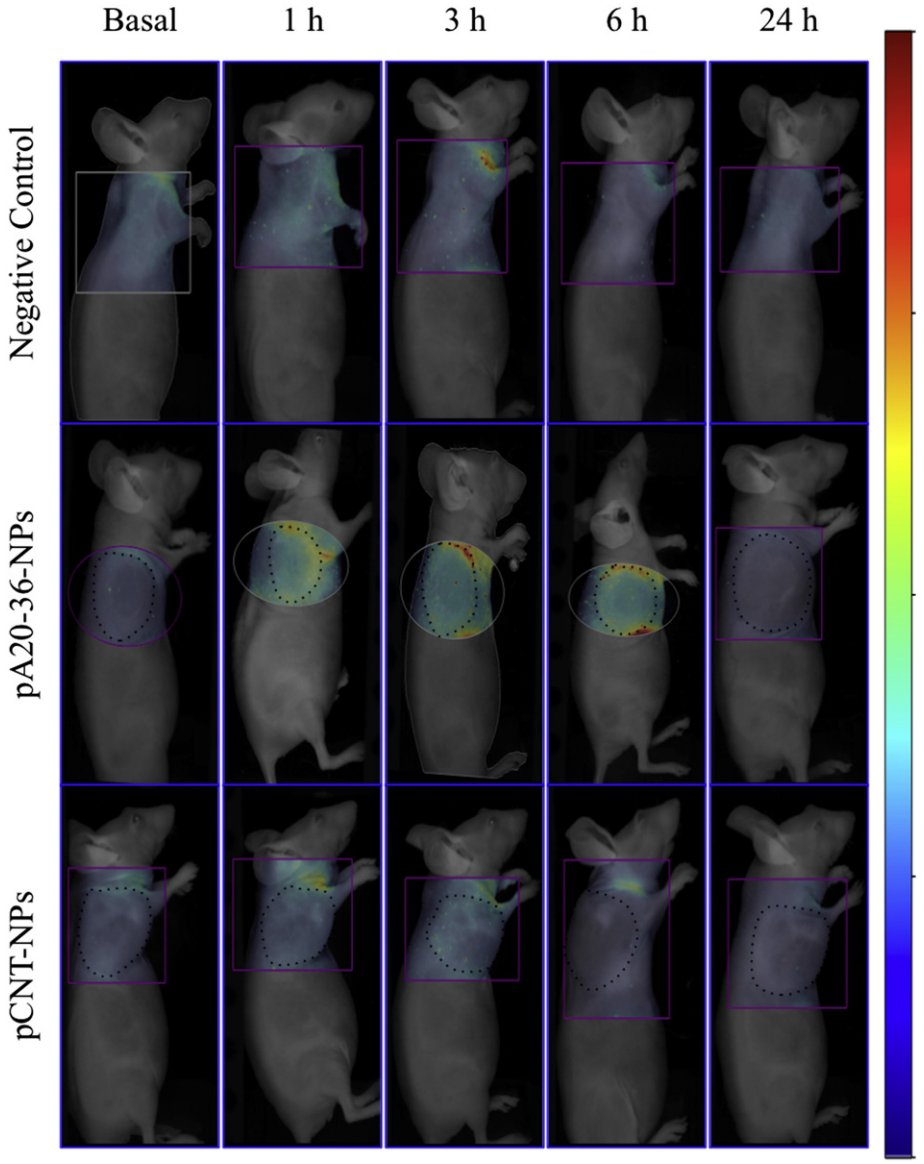

Figure 5. *In vivo* FRI results. *In vivo* two-dimensional surface fluorescence reflectance (counts/energy). Each row represents a different group, from top to bottom: negative control, pA20-36-NPs and pCNT-NPs. Each column represents a different time point, from left to right: basal (background) acquisition, and after 1, 3, 6 and 24 h of biodistribution. In the pA20-36-NPs groups, an oval region of interest was used to avoid the most non-specific signal.

Table 1
Mean ± SE of *in vivo* FMT results. Table summarizing the mean ± SE %FlS of *in vivo* FMT of the control, pA20-36-NPs and pCNT-NPs groups.

Groups	%FlS 1 h	%FlS 2 h	%FlS 3 h	%FlS 4 h	%FlS 6 h	%FlS 24 h
Negative Control	3.0 ± 0.5	5.2 ± 2.0	7.1 ± 1.7[B]	6.3 ± 2.5	1.4 ± 0.2	0.4 ± 0.2
pA20-36-NPs	20.5 ± 5.4	26.4 ± 4.7	98.5 ± 46.1[A]	22.3 ± 4.2	26.7 ± 3.8	11.0 ± 3.0
pCNT-NPs	10.2 ± 4.0	8.4 ± 2.3	8.4 ± 1.9[B]	8.4 ± 3.6	8.4 ± 1.8	2.6 ± 1.2

Statistics: A > B $P = 0.0001$.

pathology.[12,19,21] The theranostic approach presented in this work was efficient for immunotherapy of B-cell lymphoma and for multimodal imaging. Multimodality imaging is currently under exploration with the aim of obtaining important information not easily achievable using single modalities alone.[10] This work demonstrated the abilities of NPs decorated with pA20-36 to successfully perform therapy and multimodal imaging in a murine model of B-cell lymphoma.

In vivo fluorescence imaging (FRI) was selected for its high sensitivity and relatively simple procedure for substitution of other sensible techniques such as positron emission tomography (PET),[16] which still requires the use of potentially harmful

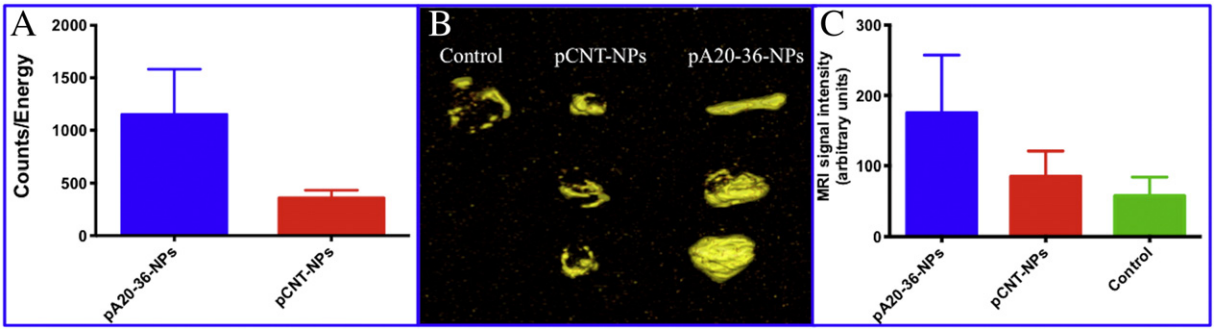

Figure 6. *Ex vivo* FRI and MRI results. (**A**) Graphic representation of the mean ± SE of the *ex vivo* fluorescent signal intensity. (**B**) Three-dimensional volume-rendering maximum intensity projection (MIP) reconstruction of the *ex vivo* MRI acquisition. Each column represents a different group, from left to right: control, pCNT-NPs and pA20-36-NPs. (**C**) Graphic representation of the mean ± SE MRI signal intensity comparisons among the three groups studied. In blue, pA20-36-NPs; in red, pCNT-NPs; in green, control.

radioactive agents. Moreover, fluorescence imaging might be easily applied for human patients, at least for scanning of superficial structures and lesions such as sentinel lymph nodes or carotid atheroma.[13,15,22] Our results demonstrated the ability of FRI to trace fluorescent NPs *in vivo* and to detect the timing of both NPs peak accumulation and their persistence in the lesion. Closer visual evaluation of the FRI images showed the highest signal intensity at the edge of the lesions, and a clear diffuse lower intensity in the whole tumor area, including surrounding tissues. Such a signal distribution might be explained with the higher concentration of blood vessels in the periphery of the tumor mass, as detected by color-Doppler HFUS imaging, whereas the deeper vascular structures were either very small or displayed a very slow flow. Nonetheless the entire tumor showed a higher signal intensity compared to controls and to pre injection images, and the different intensity between the edges and the center of the mass might be explained by the attenuation due to tumor depth, which was about 1.5 cm in height; indeed, the FRI technique is well known to reach only few millimeters in depth.[23]

Combining FRI with anatomical imaging *via* MRI facilitates interpretation of functional information. In this work, we presented a combined FRI-MRI NPs system and applied it to a murine lymphoma model. Furthermore, we compared the MRI signal intensity of pA20-36-NPs and pCNT-NPs loaded with Gd-DTPA as well as non-decorated and unloaded NPs. We used contrast-enhanced MRI to prove the ability of pA20-36-decorated NPs loaded with Gd-DTPA to selectively target the A20 lymphoma cells and preserve their cargo until they reached the target site. We chose MRI for its superior soft tissue contrast, anatomical detail and lack of ionizing radiation; this technique supplied a series of pathophysiological and functional information,[11,16] and in our experiment, this technique demonstrated the NPs persistence in the tumor region. Furthermore, the Gd-DTPA-loaded NPs used in this work were previously demonstrated as an optimal paramagnetic contrast agent *in vitro* and were proven able to boost the MRI T_1 signal by up to 6 times at a constant Gd-DTPA concentration.[20] Indeed, the modified coacervation approach proposed to obtain these NPs promotes the diffusion and exchange of metal chelates at the HA-Ch interface, leading to a peculiar environment that can boost the relaxometric properties through control of the characteristic correlation times.[24]

The use of engineered nanoparticles for imaging of tissues poses a few challenges. In particular, the HA-Ch NPs were used as carriers to load different moieties and exploited as new types of tumor-targeted drug carriers because the HA shell contains numerous active groups such as carboxylic acid or hydroxyl groups on the backbone and because hydrophobic molecules can also be encapsulated in the core.[12] In this context, the core-shell nanoparticles decorated with the pA20-36 can act as a next generation of nanoprobes, with a core that delivers biocompatible bimodal probes and a surface upon which fluorescent dye and magnetic compounds can be fused into a single nanostructure to achieve a synergistic effect. Hence, the HA NPs are a promising medical tool for targeted theranostics due in part to the specific degradation by the hyaluronidase usually highly expressed in tumors and could reduce undesirable side effects due to systemic administration of chemotherapeutics.[25] Moreover, our NPs have a negatively charged surfaces, attributed to the presence of deprotonated carboxyl groups of HA deposited on the positively charged Chitosan core. However, conjugation with A20-36 showed partial neutralization of the surface charge to −10 mV ± 5 mV. A low surface charge can improve long circulation life of nanoparticles increasing the chances of active targeting on the tumor site.

Our HA NPs did not cause major side effects, *i.e.*, none of the treated mice died during the procedures, and no weight loss or food/water consumption reductions were recorded (data not shown). We detected tachypnea or bradypnea (or a subtle tremor of the tail) during the i.v. injection in only a small fraction of subjects (approximately 1%). In all cases, slowing of the inoculation procedure led to the disappearance of the described signs. Since the aim of our experiments was to demonstrate the ability of HA-Ch NPs to effectively act as a therapeutic as well as a molecular imaging agent, we did not deepen into toxicological effects of NPs, but we did evaluate the inflammatory response in A20 cell cultures and Balb/C mice (see Supplementary Information). Further studies should be designed to verify, with the aid of fine functional, histological and biochemical analyses, the acute and long term administration effect on the major organs/body systems (*e.g.*, cardiovascular, kidney, liver).

Various NPs types have been used in targeted therapy, *e.g.*, induction of the photothermal effect or exploitation of the

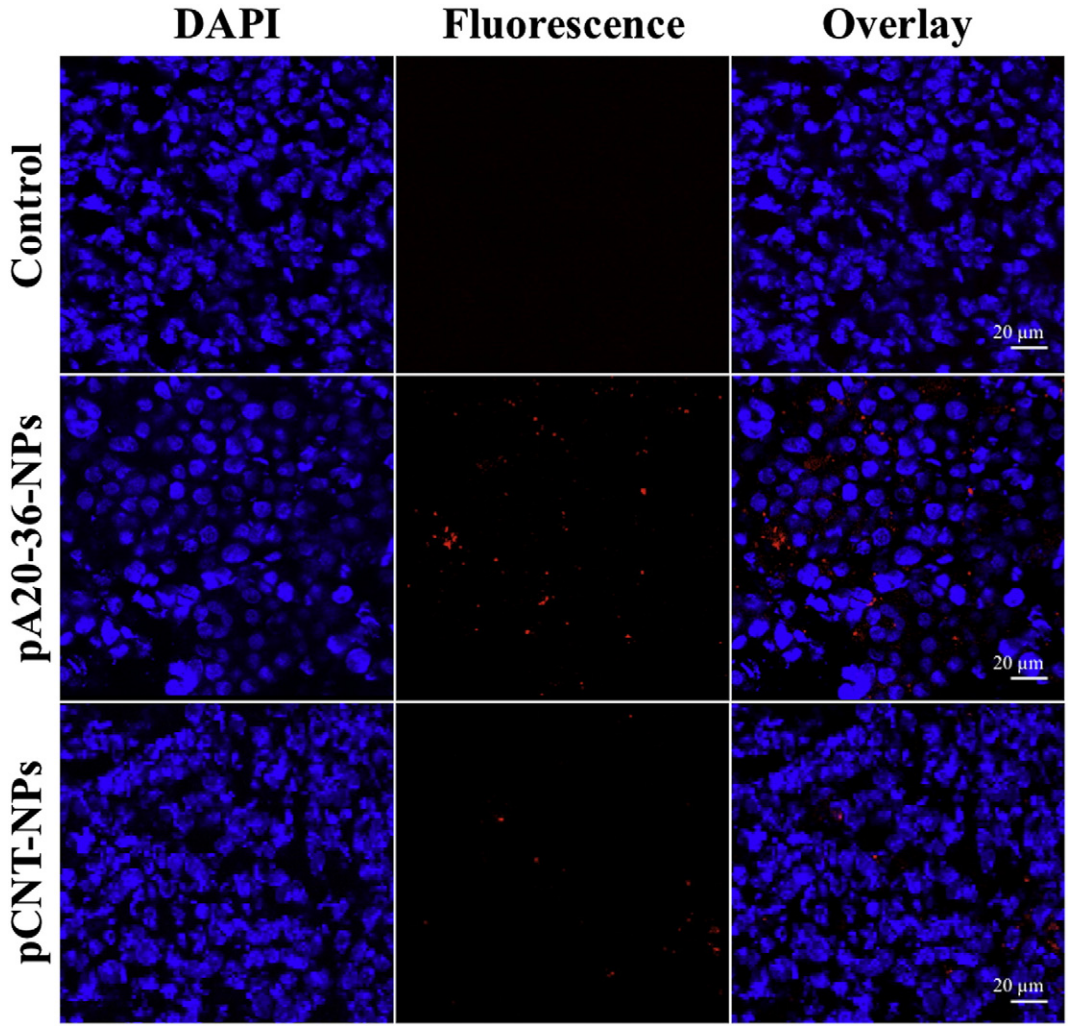

Figure 7. Confocal microscopy of *ex vivo* A20 xenograft tumors acquired with an HCX PL APO 63 × 1.40 OIL UV lens. The first column represents the DAPI stain, the second column denotes the fluorescent confocal microscopy, and the third column shows the overlay of DAPI and fluorescence. From top to bottom: first row, control, no fluorescence signal detected; second row, pA20-36-NPs, evident bright fluorescent signal; third row, pCNT-NPs, detectable low intensity.

ability of NPs to load, deliver and release chemotherapeutics in the tumor environment.[19,21,25,26] In our experiments, we selected immunotherapy mediated by the A20-36 peptide, which has been previously demonstrated to act as an apoptotic agent *in vitro* and *in vivo* to specifically target A20-cells xenograft by [^{18}F]-fluorodeoxyglucose PET imaging *in vivo*.[4]

We verified the efficacy of pA20-36 in slowing the A20 cell growth rate and reducing the tumor volume, and such effects were still evident even one week after the suspension of the therapy. This result is in agreement with that of a previous study and at a dosage lower than that previously described.[4] The choice of the lower dosage (10 mg/kg instead of 20 mg/kg) was dictated by the maximum loading ability of our NPs without administering an inadequate volume.

One open question that remains is related to why lower tumor volumes were recorded in pA20-36-NPs treated mice compared with those treated with pA20-36 alone. Even if this difference did not reach statistical significance, we hypothesize that the possible longer persistence of NPs in the tumor compared with that of pA20-36 alone might have been responsible for this effect.

We decided not to perform FRI studies during the two weeks of therapy because we could not exclude NPs accumulation in the tumor tissue, due to repeated treatments, and hence an overestimation of the imaging results. Nonetheless, we have used pA20-36-decorated ATTO680-loaded NPs for the therapy, since a different NPs preparation (*i.e.* unloaded ATTO680 NPs) procedure might have had a significant influence on results. Nonetheless, we could have performed imaging more frequently during therapy to verify the NPs accumulation assumption, but we deemed it unnecessarily stressful and invasive, at least in this phase, for the experimental mice.

In conclusion, this work demonstrates the ability of pA20-36-NPs to successfully perform therapy and multimodal imaging. Indeed, NPs offer several advantages over the peptide alone: they can be further loaded with drugs, and they appear to be the easiest approach to performing theranostics and multimodality imaging,

with the choice of the most suitable imaging agents depending on the tumor type. Finally, it is presumable that intravenous administration of pA20-36-decorated biopolymers might allow targeting of multiple tumor niches in the case of diffuse systemic lymphoma.

Acknowledgment

Authors wish to thank the technical assistance of dott. D. Montanaro (CEINGE, Biotecnologie Avanzate s.c.ar.l., Napoli, Italia) and dott. E. Romano.

Appendix A. Supplementary data

Supplementary data to this article can be found online at https://doi.org/10.1016/j.nano.2017.11.016.

References

1. Stevenson FK, Spellerberg M, Smith JL. Monoclonal immunoglobulin light chain in urine of patients with B lymphocytic disease: its source and use as a diagnostic aid. *Br J Cancer* 1983;**47**(5):607-12.
2. Bergenbrant S, Yi Q, Osterborg A, Björkholm M, Osby E, Mellstedt H, et al. Modulation of anti-idiotypic immune response by immunization with the autologous M-component protein in multiple myeloma patients. *Br J Haematol* 1996;**92**(4):840-6.
3. Korde N, Maric I. Myelomagenesis: capturing early microenvironment changes. *Semin Hematol* 2011;**48**(1):13-21.
4. Palmieri C, Falcone C, Iaccino E, Tuccillo FM, Gaspari M, Trimboli F, et al. In vivo targeting and growth inhibition of the A20 murine B-cell lymphoma by an idiotype-specific peptide binder. *Blood* 2010;**116**(2):226-38.
5. Knittelfelder R, Riemer AB, Jensen-Jarolim E. Mimotope vaccination—from allergy to cancer. *Expert Opin Biol Ther* 2009;**9**(4):493-506.
6. Linnemann T, Tumenjargal S, Gellrich S, Wiesmüller K, Kaltoft K, Sterry W, et al. Mimotopes for tumor-specific T lymphocytes in human cancer determined with combinatorial peptide libraries. *Eur J Immunol* 2001;**31**(1):156-65.
7. Tumenjargal S, Gellrich S, Linnemann T, Muche JM, Lukowsky A, Audring H, et al. Anti-tumor immune responses and tumor regression induced with mimotopes of a tumor-associated T cell epitope. *Eur J Immunol* 2003;**33**(11):3175-85.
8. Leo N, Shang Y, Yu JJ, Zeng X. Characterization of self-assembled monolayers of peptide Mimotopes of CD20 antigen and their binding with rituximab. *Langmuir* 2015;**31**(51):13764-72.
9. Zhao N, Williams TM, Zhou Z, Fronczek FR, Sibrian-Vazquez M, Jois SD, et al. Synthesis of BODIPY-peptide conjugates for fluorescence labeling of EGFR overexpressing cells. *Bioconjug Chem* 2017;**28**(5):1566-79.
10. Cherry SR. Multimodality in vivo imaging systems: twice the power or double the trouble? *Annu Rev Biomed Eng* 2006;**8**:35-62.
11. Auletta L, Gramanzini M, Gargiulo S, Albanese S, Salvatore M, Greco A. Advances in multimodal molecular imaging. *Q J Nucl Med Mol Imaging* 2017;**61**(1):19-32.
12. Liang X, Fang L, Li X, Zhang X, Wang F. Activatable near infrared dye conjugated hyaluronic acid based nanoparticles as a targeted theranostic agent for enhanced fluorescence/CT/photoacoustic imaging guided photothermal therapy. *Biomaterials* 2017;**132**:72-84.
13. Mulder WJ, Griffioen AW, Strijkers GJ, Cormode DP, Nicolay K, Fayad ZA. Magnetic and fluorescent nanoparticles for multimodality imaging. *Nanomedicine (Lond)* 2007;**2**(3):307-24.
14. Talanov VS, Regino CA, Kobayashi H, Bernardo M, Choyke PL, Brechbiel MW. Dendrimer-based nanoprobe for dual modality magnetic resonance and fluorescence imaging. *Nano Lett* 2006;**6**(7):1459-63.
15. Jaffer FA, Libby P, Weissleder R. Optical and multimodality molecular imaging: insights into atherosclerosis. *Arterioscler Thromb Vasc Biol* 2009;**29**(7):1017-24.
16. Wang Y, Chen J, Yang B, Qiao H, Gao L, Su T, et al. In vivo MR and fluorescence dual-modality imaging of atherosclerosis characteristics in mice using Profilin-1 targeted magnetic nanoparticles. *Theranostics* 2016;**6**(2):272-86.
17. Chen Q, Shang W, Zeng C, Wang K, Liang X, Chi C, et al. Theranostic imaging of liver cancer using targeted optical/MRI dual-modal probes. *Oncotarget* 2017;**8**(20):32741-51.
18. Greco A, Albanese S, Auletta L, De Carlo F, Salvatore M, Howard CM, et al. Advances in molecular preclinical therapy mediated by imaging. *Q J Nucl Med Mol Imaging* 2017;**61**(1):76-94.
19. Hwang JY, Park J, Kang BJ, Lubow DJ, Chu D, Farkas DL, et al. Multimodality imaging in vivo for preclinical assessment of tumor-targeted doxorubicin nanoparticles. *PLoS ONE* 2012;**7**(4)e34463.
20. Vecchione D, Grimaldi AM, Forte E, Bevilacqua P, Netti PA, Torino E. Hybrid Core-Shell (HyCoS) nanoparticles produced by complex coacervation for multimodal applications. *Sci Rep* 2017;**7**:45121.
21. Zhou H, Hou X, Liu Y, Zhao T, Shang Q, Tang J, et al. Superstable magnetic nanoparticles in conjugation with near- infrared dye as a multimodal theranostic platform. *ACS Appl Mater Interfaces* 2016;**8**:4424-33.
22. Kircher MF, Mahmood U, King RS, Weissleder R, Josephson L. A multimodal nanoparticle for preoperative magnetic resonance imaging and intraoperative optical brain tumor delineation. *Cancer Res* 2003;**63**(23):8122-5.
23. Ntziachristos V, Bremer C, Weissleder R. Fluorescence imaging with near-infrared light: new technological advances that enable in vivo molecular imaging. *Eur Radiol* 2003;**13**:195-208.
24. Ponsiglione AM, Russo M, Netti PA, Torino E. Impact of biopolymer matrices on relaxometric properties of contrast agents. *Interface Focus* 2016;**6**(6):20160061.
25. Li W, Zheng C, Pan Z, Chen C, Hu D, Gao G, et al. Smart hyaluronidase-actived theranostic micelles for dual-modal imaging guided photodynamic therapy. *Biomaterials* 2016;**101**:10-9.
26. Gao M, Fan F, Li D, Yu Y, Mao K, Sun T, et al. Tumor acidity-activatable TAT targeted nanomedicine for enlarged fluorescence/magnetic resonance imaging-guided photodynamic therapy. *Biomaterials* 2017;**133**:165-75.